Modeling and characterization of a cantilever-based near-field scanning microwave impedance microscope

K. Lai, W. Kundhikanjana, M. Kelly, and Z. X. Shen
Department of Applied Physics and Geballe Laboratory for Advanced Materials, Stanford University, Stanford, California 94305, USA

(Received 14 January 2008; accepted 28 May 2008; published online 25 June 2008)

This paper presents a detailed modeling and characterization of a microfabricated cantilever-based scanning microwave probe with separated excitation and sensing electrodes. Using finite-element analysis, we model the tip-sample interaction as small impedance changes between the tip electrode and the ground at our working frequencies near 1 GHz. The equivalent lumped elements of the cantilever can be determined by transmission line simulation of the matching network, which routes the cantilever signals to 50 Ω feed lines. In the microwave electronics, the background common-mode signal is canceled before the amplifier stage so that high sensitivity (below 1 aF capacitance changes) is obtained. Experimental characterization of the microwave microscope was performed on ion-implanted Si wafers and patterned semiconductor samples. Pure electrical or topographical signals can be obtained from different reflection modes of the probe. © *2008 American Institute of Physics.* [DOI: 10.1063/1.2949109]

I. INTRODUCTION

A new paradigm of electrodynamic measurements, known as near-field microscopy, has emerged in the past few decades to study electromagnetic properties down to a length scale much smaller than the free-space wavelength.[1] Using this technique, submicron spatial resolution can be achieved at low frequencies, such as in the microwave regime.[1–5] Here, a sharp near-field probe tip, being an extension of transmission lines or waveguides that carry propagating microwaves, locally interacts with the specimen under test.[2] As the probe scans over the sample surface, variation of the local sample property results in changes of the impedance between the probe tip and ground, which are then detected and recorded to form near-field images, with a spatial resolution comparable to the curvature of the tip apex. Because of the potential applications in electron physics, material science, and biological studies, several groups have developed near-field scanning microwave microscopes as scientifically useful instruments.[6–11]

The implementation of near-field microwave imaging, however, exhibits several technical challenges. In order to achieve high spatial resolution, the probe has to be brought very close to or in contact with the sample. The fabrication of sharp and robust near-field probes, especially in batch production, is a nontrivial process. Second, the signal from the highly localized tip-sample interaction is usually very small, demanding exceptional sensitivity and stability of the detection system. Thirdly, the near-field results are far more difficult to interpret than the conventional far-field data. The signal here is often a complicated convolution between the probe geometry, especially near the tip end, and the sample property, including the real electromagnetic response and the surface topography.[1–5] Finally, spurious signal can occur due to insufficient shielding of any nonlocal stray field and the propagating far-field component. As a result, careful design of the tip structure and the detection scheme, as well as extensive characterization of the system, is imperative for the application of near-field microwave imaging.

In a recent publication, we reported the design and preliminary results of a microwave impedance microscope (MIM).[12] Based on commercial atomic force microscope (AFM) platforms, the MIM resembles the well established scanning capacitance microscope (SCM) technique in that both detection electronics work at a frequency near 1 GHz.[13,14] Our implementation, on the other hand, has several advantages over SCM and other near-field microwave microscopes discussed in literature. Microwave imaging in general does not require a back electrode on the specimen and the modulation of the tip-sample capacitance, making possible general-purpose imaging on a variety of samples. Both the real and imaginary components of the dielectric property, usually not obtained in SCM, are measured in our microwave electronics, as detailed below. Compared to other cantilever-based microwave microscope designs,[15,16] our probe uses metal lines for the electrodes to greatly reduce the loss in doped Si traces. The background signal is canceled before amplification to ensure large power gain and high sensitivity. More importantly, our probe is unique in that, besides the sharp sensing electrode, a second electrode surrounding the tip is also present on the cantilever. Various operation modes, including transmission between both electrodes and reflection from either electrode, can be used to achieve different sample information. In this paper, we present a detailed modeling of the contrast mechanism and characterization of the instrument using patterned semiconductor structures. Many experimental findings demonstrated here should lead to interesting applications of the technique.

II. SYSTEM CHARACTERIZATION

Figure 1(a) shows a picture of the MIM probe fabricated by microelectromechanical systems technology.[12] A sche-

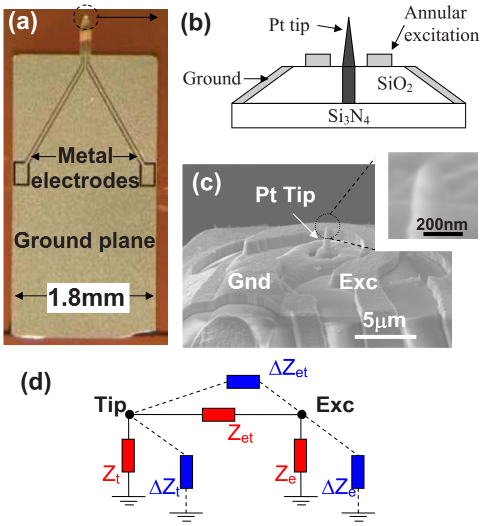

FIG. 1. (Color online) (a) Microfabricated microwave probe with two aluminum electrodes and the ground plane patterned on the Si nitride cantilever. (b) Schematic drawing of the layer structure near the probe end. (c) SEM image near the probe end. The apex of the FIB deposited Pt tip is shown in the inset. (d) Lumped-element circuit model of the probe, showing the total and small changes in the impedances.

matic of the tip structure is shown in Fig. 1(b). The annular excitation electrode and the tip electrode, formed after microfabrication by focused-ion beam (FIB) deposition of Pt, can be seen in the scanning electron microscope (SEM) image in Fig. 1(c). Since the dimension of the entire chip is much smaller than the free-space wavelength (30 cm) at our working frequency of 1 GHz, the lumped-element circuit description is appropriate to represent the probe, with three discrete impedances $-Z_e$ between excitation and ground, Z_t between tip and ground, and Z_{et} between excitation and tip—across the relevant electrodes. Due to the tip-sample interaction, the small impedance changes [ΔZ_e, ΔZ_t, and ΔZ_{et} in Fig. 1(d)] during the scanning contain local sample information. A complete understanding of the contrast mechanism of our microscope, therefore, requires knowledge of both near-field interaction and microwave electronics. In the following, we detail the procedure of system characterization in three steps. First (Sec. II A), using finite-element analysis (FEA), we model the tip-sample interaction as small impedance changes (ΔZ_e, ΔZ_t, and ΔZ_{et}). Second (Sec. II B), the microwave circuitry response due to these small ΔZ's is calculated by transmission line simulation. Finally (Sec. II C), the gain of the electronics is determined so that the contrast in the microwave images can be directly compared with our modeling results. The reference of the homodyne detection also has to be properly adjusted in order to achieve the phase information.

A. Tip-sample interaction

Since the relevant length scale of the tip-sample interaction is five orders of magnitude smaller than the wavelength, it is justified[3] that the complicated near-field interaction can be reduced to two parameters—the real and imaginary parts of the effective tip impedance. Furthermore, any stray field contribution from the nontip part, e.g., the Al electrodes, is

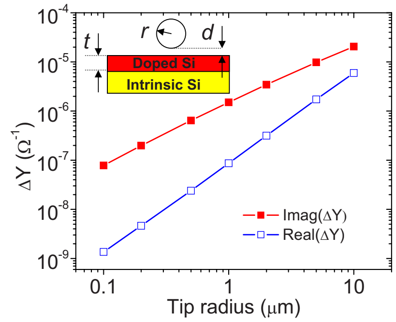

FIG. 2. (Color online) COMSOL results of the admittance contrast ΔY between undoped Si and the structure in the inset, a $t=1$ μm doped (1 Ω cm) Si film on intrinsic substrate. Both real and imaginary parts of ΔY are plotted as a function of the tip radius r. A very thin air gap d is assumed between the tip and the sample.

essentially constant during a single scan. One can therefore simulate the impedance changes and quantitatively model the relative contrast in the microwave images.

Of the three impedance changes, ΔZ_t represents the most localized tip-sample interaction. Approximating the tip as a conducting sphere with the same diameter at its apex, several groups have performed numerical or analytical analysis to compute this tip-sample impedance change.[17–20] Using empirical calibrations, good agreements with experiments have been obtained, showing the ability of quantitative study of materials in the near field. However, most existing microwave microscopes utilize chemically etched metal wires as the tips, with a diameter in the order of 10 μm.[19–22] For better spatial resolution, our FIB deposited Pt tip has a much smaller diameter 100–200 nm, as shown in the inset of Fig. 1(b). Due to the much sharper tip, any meaningful calculation of ΔZ_t requires extensive knowledge of the exact tip shape and the condition of the sample surface, e.g., the thickness of an unintended contamination layer.

Figure 2 shows the simulation results from a FEA software COMSOL3.4 (Ref. 23) that directly computes the admittance Y (inverse impedance $1/Z$) between two arbitrarily shaped electrodes inside a dielectric or conductive medium. The two dimensional axisymmetric quasistatic mode and time-harmonic ($f=1$ GHz) analysis are employed. The tip is assumed to be a perfectly conducting sphere with radius r ranging from 0.1 to 10 μm. For demonstration purposes, we calculate the admittance contrast ΔY between intrinsic silicon (dielectric constant $\varepsilon_r=12$, conductivity ~ 0) and the structure sketched in the inset of Fig. 2, a thin doped Si film (thickness $t=1$ μm, $\varepsilon_r=12$, resistivity $\rho=1$ Ω cm) on top of the intrinsic substrate. A thin air gap $d=1$ nm is assumed between the tip and the sample to avoid problems due to finite mesh size. The results, plotted in Fig. 2, show several important features of the near-field tip-sample interaction. As a measure of the capacitive coupling, the imaginary part of the contrast signal roughly scales with the tip diameter, demanding a very sensitive detection scheme when high spatial resolution is required. The real or resistive component of the contrast reduces even faster as a function of the tip size. As a result, for small radii in particular, careful preservation of the tip condition and extensive calibration effort are imperative. For example, a set of standard samples, as we discuss below,

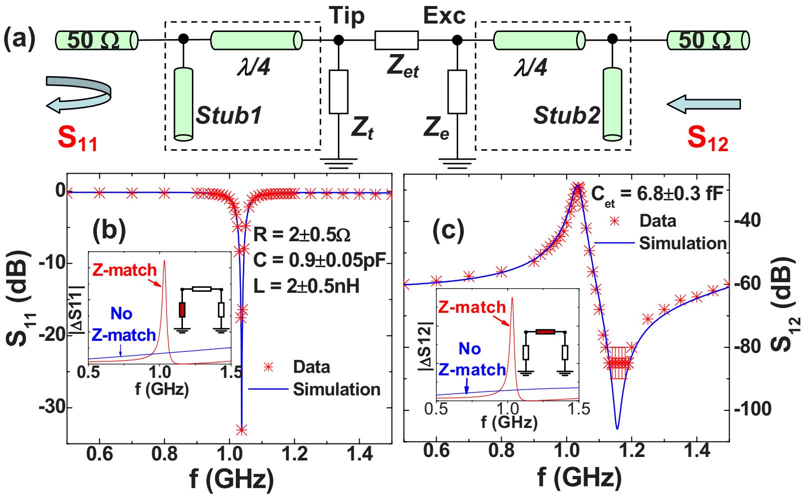

FIG. 3. (Color online) (a) Impedance matching section. A λ/4 cable and a tuning stub (inside the dashed boxes) form the interface between the probe and the 50 Ω feed lines. (b) Measured S_{11} data and a fit to the transmission line analysis. The inset shows $|\Delta S_{11}|$ for a given $\Delta C_t = 1$ aF, with and without impedance matching. (c) Measured S_{12} data and the transmission line simulation result, and $|\Delta S_{12}|$ for $\Delta C_{et} = 1$ aF in the inset.

is needed to calibrate the system. Assuming the system, including the tip condition, remains stable, these interaction parameters can then be used to determine unknown samples quantitatively. Crosscheck of the system response from the standard samples is also necessary before and after the experiment.

When the tip is in contact with the sample, the overall distance between the big excitation electrode and the sample follows the surface topography, resulting in a mostly capacitive ΔZ_e. In other words, the reflection signal from the excitation electrode shows essential the geometrical features, as one would normally obtain from the AFM function. The capacitance change, $\Delta C = \varepsilon_0 (A/h)\Delta h^2 \sim 20$ aF, can be easily estimated from the simple parallel-plate capacitor approximation, where $A \sim 100\ \mu m^2$ is the area of the annular electrode, $h = 2\ \mu m$ the tip height above it, and a small particle with $\Delta h = 100$ nm on the sample.

Finally, transmission measurements can be performed when the microwave power is supplied by one electrode and collected by the other. Because the coupling impedance Z_{et} is much larger than Z_e or Z_t, the power level in the sensing electrode is much lower than that in the excitation electrode, so the common-mode signal and shot noise are greatly reduced. In this configuration, all three impedance changes in Fig. 1(c) affect the final signal and one can again use finite-element analysis to model ΔZ_{et}.[12]

B. Impedance matching

As stated before, the fabricated microwave probe can be modeled as discrete lumped elements. Neglecting the small geometrical differences between the two electrodes at the tip end, we determined that Z_e or Z_t is equivalent to the series of a resistor $R \sim 2\ \Omega$, an inductor $L \sim 2$ nH, and a capacitor $C \sim 1$ pF to ground, with the capacitor dominating the total impedance at $f \sim 1$ GHz. Because of the large mismatch between $Z_e(Z_t)$ and the transmission line impedance $Z_0 = 50\ \Omega$, microwave power will not be delivered to the probe if it is directly connected to the feed line, and the detection of small impedance variations is not feasible.

Several schemes are available to achieve impedance matching in existing microwave microscopes. In our MIM, the tip is first attached to the end of a λ/4 section of a transmission line to form a resonator, as seen in Fig. 3(a). The resonator is then critically coupled to the feed line by a parallel open-end tuning stub. Nearly perfect matching, indicated by a small reflection coefficient $S_{11} < -30$ dB, is easily obtained with this tunable stub. To minimize the force and vibration on the AFM platform, we use very flexible Astroboa-flex® III microwave cables for both the λ/4 line and the tuning stub. The nominal group velocity is 2.1×10^8 m/s in the cable and the loss is 2.4 dB/m.

Figure 3(b) shows a typical reflection coefficient S_{11} curve taken by HP 8510B network analyzer. Very good impedance matching is achieved at $f = 1.035$ GHz for $l_{\lambda/4} = 4.4$ cm and $l_{stub} = 4.3$ cm. The transmission line simulation result using the measured length and propagation constant of the cable is also shown in Fig. 3(b). In fact, Z_e and Z_t can be verified this way by the good fit to standard transmission line formula at various stub length (not shown). Besides, by fitting the S_{12} data, one can also determine the coupling capacitance $C_{et} \sim 7$ fF.

Finally, given a small impedance change at the tip, the contrast signal from the matching section, $\Delta V = V_{in} \times \Delta S_{11}$ (reflection) or $V_{in} \times \Delta S_{12}$ (transmission),[24] can be simulated using the same transmission line analysis. Assuming 1 aF capacitive perturbation in either Z_t or Z_{et}, we show the calculated ΔS_{11} and ΔS_{12} in the inset of Figs. 3(b) and 3(c). Compared to the situation without the matching section, the signal level is about an order of magnitude higher when Z_e and Z_t are matched to the 50 Ω line impedance.

C. Microwave circuitry

Figure 4 shows the block diagram of the detection microwave circuit, which was detailed in Ref. 12. The reflected or transmitted signal from the matching network contains a large background, which could saturate the amplifiers. In order to sensitively pick up the small contrast from this large background or common-mode signal, we combine a cancellation signal, equal in magnitude but opposite in phase, with the input signal at the amplifier input before a scan. The contrast signal within the scanned area is then amplified by the rf amplifier, demodulated by an IQ mixer, and amplified again in the dc stage. A feedback from the dc output with a long time constant (10 s) controls the variable attenuators in

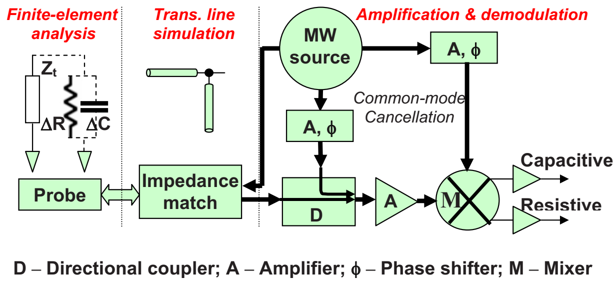

FIG. 4. (Color online) Block diagram of the microwave detection circuitry. The probe signal due to impedance change, through impedance matching, is null before the scan. The contrast signal is then amplified and demodulated to form near-field images.

the cancellation circuit to suppress the system drift due to, e.g., temperature instability. At our usual 0.5 Hz line scan rate, the cancellation feedback functions properly. For system drift at even longer time scale, the average value of each line scan is subtracted to remove the slow varying background. The total gain, including rf and dc, is about 110 dB at 1 KHz bandwidth. Assuming −20 dBm (10 μW) input power, a 1 aF capacitance change at the tip produces ~15 mV dc output signal, which is comparable to the thermal noise. Therefore, when properly tuned, our microscope is sensitive to the local impedance change down to the aF level.

The two outputs of the IQ mixer are 90° out of phase. For a sample with only dielectric contrast, i.e., a purely imaginary ΔZ, one can adjust the phase of the mixer reference so that the contrast appears only in one channel, the capacitive channel. The other channel, the resistive channel, then corresponds to the real part of ΔZ. Similar to other microwave microscopes, no contrast will show up in the resistive channel if the sample is insulating or a perfect metal.[21]

III. EXPERIMENTAL RESULTS

As discussed before, the MIM is a very sensitive tool to detect local tip-sample impedance changes down to the submicron length scale. Depending on the specific mode, the contrast may originate from the local electrical properties (tip reflection), the sample topography (excitation reflection), or a combination of both (transmission) with much reduced power at the tip electrode. In the following, we show microwave images on several patterned semiconductor samples. The transmission data have been explained in Ref. 12 and results from reflection measurements will be the focus of this study.

A. Reflection from the tip electrode

A set of topography-free samples was fabricated to characterize pure electrical responses from the tip electrode. As shown in Fig. 5(a), 1×10^{12} cm^{-2} phosphorus ions were implanted into repeated 4×4 μm^2 windows on a high-resistivity (HR) ($\rho>1000$ Ω cm) p-Si substrate. The dose was kept low comparing to other work ($>10^{14}$ cm^{-2}) (Refs. 21, 25, and 26) to demonstrate the high sensitivity of the MIM. The dopants were then activated at 1100 °C for

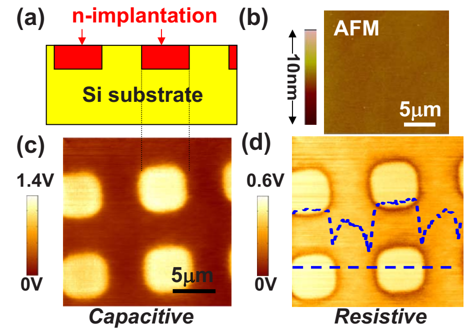

FIG. 5. (Color online) (a) Schematic of the implantation sample. (b) AFM image of the topography-free sample surface. (c) and (d) Two orthogonal, capacitive and resistive, microwave images (reflection from the tip electrode), with a line cut in the resistive channel image. The color bar corresponds to 1.4 V full scale in (c) and 0.6 V in (d).

30 min, resulting in a surface doping level $\sim2\times10^{16}$ cm^{-3}. Microwave images from two orthogonal channels in Figs. 5(c) and 5(d) show clear contrast between the doped and undoped regions. We emphasize that such contrast is purely electrical because the conventional AFM image, taken by a Veeco Digital Instruments Multimode AFM, shows featureless topography, as seen in Fig. 5(b). The contrast mostly shows up in the capacitive channel since the implanted region results in a small shunt resistor that shorts the tip-to-ground capacitance. For the resistive channel image in Fig. 5(d), a line cut shows that the signal is nonmonotonic across the boundary, presumably the depletion region, between the p substrate and the n-type implanted dots.

To compare with the modeling results, identical patterning and implantation process were employed on three p-type Si substrates, labeled as Si-L ($\rho=21$ Ω cm, $p\sim6.2\times10^{14}$ cm^{-3}), Si-K ($\rho=11$ Ω cm, $p\sim1.2\times10^{15}$ cm^{-3}), and Si-I ($\rho=0.4$ Ω cm, $p\sim4.2\times10^{16}$ cm^{-3}), where the resistivity was determined by four-probe measurements. The microwave images in the capacitive channel are shown in Fig. 6(a). The contrast between the implanted dots and the substrate follows nicely with the substrate resistivity, and reverses the sign for Si-I, in which the n-type dopants do not fully compensate the background p doping. In the other channel (not shown), similar ringlike structure is observed

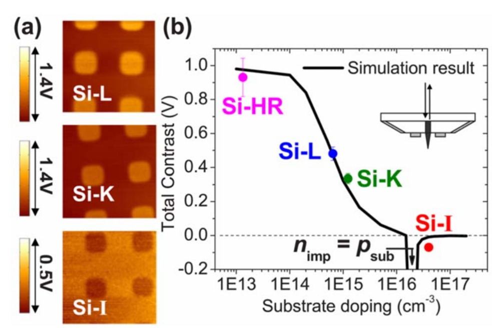

FIG. 6. (Color online) (a) 20×20 μm^2 microwave images (capacitive channel) of three Si samples with the same implantation dose as that in Fig. 5. (b) Simulated total contrast signal between the substrate and the implanted region. The contrast turns negative when the p-type substrate doping level is higher than the surface n-type implantation density. The experimental data are also included for comparison. The schematic in the inset shows that the tip reflection signal is measured.

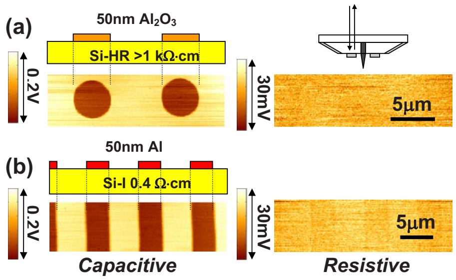

FIG. 7. (Color online) Microwave images taking reflection signals from the excitation electrode. The sample structures are schematically shown: (a) 50 nm Al_2O_3 on Si-HR and (b) 50 nm Al on Si-*I*. The full color scale is 200 mV for the capacitive channel and 30 mV for the resistive channel. The inset shows schematically that the reflection from the annular electrode is measured.

around the dots for Si-*L* and Si-*K*, but not Si-*I*. The simulation result of the total contrast signal (vector sum of the two orthogonal channels) is shown in Fig. 6(b) as a function of the substrate doping density. For simplicity, a uniform doping profile 2×10^{16} cm^{-3} for the top 0.5 μm is used in the modeling. Good agreement can be obtained between the experimental data and the simulation, in which the following parameters are assumed, tip radius $r=100$ nm, native oxide thickness $d=1$ nm, microwave input power $P=10$ μW, and total gain $G=110$ dB.[27] To model the tip/sample interaction, we assume a small tip-sample separation (1 nm) to avoid singularities in the finite-element computation. For quantitative studies, extensive calibration of the system using standard kits and careful preparation of the tip and the sample surface will be imperative.

Finally, it is worth pointing out that all images were taken with all light sources turned off. In the presence of significant illumination above the Si band gap, the photoconductivity of the sample can be so prominent that contrast between the substrate and the implanted region is largely washed out. This interesting photoconductivity effect is currently under intensive study.

B. Reflection from the annular electrode

Figure 7 shows the reflection images from the large electrode. Several samples was fabricated and measured to demonstrate the dominant dependence on topography of this mode. For the two samples here, the electrical contrast is very different and the tip reflection shows ~0.1 V contrast for Al_2O_3 on Si-HR and ~1.2 V for Al on Si-*I* (not shown). The reflection from the annular electrode, on the other hand, shows the same contrast ~160 mV only in the capacitive channel. In fact, very similar contrast of 140 ± 30 mV is observed for many test samples with 40–60 nm step height, independent of the sample dielectric constant, conductivity, and the presence of illumination. This contrast signal is also consistent with a simple parallel-plate calculation, which expects ~150 mV for 50 nm step height at the setting of our electronics. We emphasize that, unlike the usual AFM, this mode does not need any optics to measure the sample topography. With sufficient gain and stability, this signal can be utilized to maintain a constant sensor height in the noncontact mode.

IV. CONCLUSION

To summarize, we have developed a procedure to systematically study the contrast mechanism of a cantilever-based scanning microwave probe. The impedance change due to tip-sample interaction and the *S* parameters of the matching network can be modeled by finite-element analysis and transmission line simulation, respectively. Our current electronics is optimized for relative imaging rather than absolute measurements. Using a set of ion-implanted Si samples with tip reflection, we have characterized a pure electrical contrast signal that agrees with the modeling. The reflection signal from the annular excitation electrode, consistent with the simulation results, shows essentially the sample topography. Since the tip electrode is most sensitive to local electrical properties and the annular electrode to topography, combining signals from both electrodes can potentially deconvolve the electrical and topographical information, a major problem with earlier microwave instruments.

ACKNOWLEDGMENTS

This research was funded by the seed grant in Center of Probing the Nanoscale (CPN), Stanford University, with partial support from a gift grant of Agilent Technologies, Inc., and DOE Contract No. DE-FG03-01ER45929-A001. CPN is a NSF NSEC, NSF Grant No. PHY-0425897. The cantilevers and the ion-implantation samples were fabricated in Stanford Nanofabrication Facility (SNF) by A. M. Fitzgerald and B. Chui in A. M. Fitzgerald and Associates, LLC, San Carlos, CA. The authors acknowledge technical support from Agilent Technologies, Inc.

[1] B. T. Rosner and D. W. van der Weide, Rev. Sci. Instrum. **73**, 2505 (2002).
[2] M. Fee, S. Chu, and T. W. Hansch, Opt. Commun. **69**, 219 (1989).
[3] S. M. Anlage, V. V. Talanov, and A. R. Schwartz, in *Scanning Probe Microscopy: Electrical and Electromechanical Phenomena at the Nanoscale*, edited by S. V. Kalinin and A. Gruverman (Springer, New York, 2006), pp. 207–245.
[4] S. M. Anlage, D. E. Steinhauer, B. J. Feenstra, C. P. Vlahacos, and F. C. Wellstood, in *Microwave Superconductivity*, edited by H. Weinstock and M. Nisenoff (Kluwer, Amsterdam, 2001), pp. 239–269.
[5] M. Tabib-Azar, Rev. Prog. Quant. Nondestr. Eval. **20**, 400 (2001).
[6] C. P. Vlahacos, R. C. Black, S. M. Anlage, A. Amar, and F. C. Wellstood, Appl. Phys. Lett. **69**, 3272 (1996).
[7] M. Tabib-Azar, D.-P. Su, A. Pohar, S. R. LeClair, and G. Ponchak, Rev. Sci. Instrum. **70**, 1725 (1999).
[8] M. Golosovsky and D. Davidov, Appl. Phys. Lett. **68**, 1579 (1996).
[9] J. Bae, T. Okamoto, T. Fujii, K. Mizuno, and Tatsuo Nozokido, Appl. Phys. Lett. **71**, 3581 (1997).
[10] S. Hong, J. Kim, W. Park, and K. Lee, Appl. Phys. Lett. **80**, 524 (2002).
[11] T. Wei, X.-D. Xiang, W. G. Wallace-Freedman, and P. G. Schultz, Appl. Phys. Lett. **68**, 3506 (1996).
[12] K. Lai, M. B. Ji, N. Leindecker, M. A. Kelly, and Z. X. Shen, Rev. Sci. Instrum. **78**, 063702 (2007).
[13] R. C. Palmer, E. J. Denlinger, and H. Kawamota, RCA Rev. **43**, 194 (1982).
[14] V. V. Zavyalov, J. S. McMurray, and C. C. Williams, Rev. Sci. Instrum. **70**, 158 (1999).
[15] D. W. van der Weide, Appl. Phys. Lett. **70**, 677 (1997); B. T. Rosner, T. Bork, V. Agrawal, and D. W. van der Weide, Sens. Actuators, A **102**, 185 (2002).
[16] M. Tabib-Azar and Y. Wang, IEEE Trans. Microwave Theory Tech. **52**, 971 (2004).
[17] A. Imtiaz, M. Pollak, S. M. Anlage, J. D. Barry, and J. Melngailis, J. Appl. Phys. **97**, 044302 (2005).
[18] C. Gao, B. Hu, P. Zhang, M. Huang, W. Liu, and I. Takeuchi, Appl. Phys.

Lett. **84**, 4647 (2004), and references therein.
[19] Z. Wang, M. A. Kelly, Z.-X. Shen, G. Wang, X.-D. Xiang, and J. T. Wetzel, J. Appl. Phys. **92**, 808 (2002).
[20] J. H. Lee, S. Hyun, and K. Char, Rev. Sci. Instrum. **72**, 1425 (2001).
[21] A. Imtiaz and S. M. Anlage, Ultramicroscopy **94**, 209 (2003); J. Appl. Phys. **100**, 044304 (2006).
[22] Z. Wang, M. A. Kelly, Z.-X. Shen, L. Shao, W.-K. Chu, and H. Edwards, Appl. Phys. Lett. **86**, 153118 (2005).
[23] COMSOL, Inc., Palo Alto, CA.
[24] R. Wang, F. Li, and M. Tabib-Azar, Rev. Sci. Instrum. **76**, 054701 (2005), and references therein.
[25] A. Tselev, S. M. Anlage, H. M. Christen, R. L. Moreland, V. V. Talanov, and A. R. Schwartz, Rev. Sci. Instrum. **74**, 3167 (2003).
[26] A. Imtiaz, S. M. Anlage, J. D. Barry, and J. Melngailis, Appl. Phys. Lett. **90**, 143106 (2007).
[27] The actual tip-sample interface is also affected by the work function difference and small rf oscillating potential. Such effect will slightly modify the sample surface and is not included in our current simulation.